Research Article | Vol. 30, No. 7 / 28 Mar 2022 / Optics Express 11181
Optics EXPRESS

Quantitative near-field characterization of surface plasmon polaritons on monocrystalline gold platelets

LAURA N. CASSES,[1,2,3] KORBINIAN J. KALTENECKER,[1,2,4] SANSHUI XIAO,[1,2,3] MARTIJN WUBS,[1,2,3] AND NICOLAS STENGER[1,2,3,*]

[1]Department of Photonics Engineering, Technical University of Denmark, 2800 Kongens Lyngby, Denmark
[2]Center for Nanostructured Graphene, Technical University of Denmark, 2800 Kongens Lyngby, Denmark
[3]Center for Nanophotonics, Technical University of Denmark, 2800 Kongens Lyngby, Denmark
[4]Current address: Attocube Systems AG, Eglfinger Weg 2, 85540 Haar, Germany
*niste@fotonik.dtu.dk

Abstract: Near-field microscopy allows for visualization of both the amplitude and phase of surface plasmon polaritons (SPPs). However, their quantitative characterization in a reflection configuration is challenging due to complex wave patterns arising from the interference between several excitation channels. Here, we present near-field measurements of SPPs on large monocrystalline gold platelets in the visible. We study systematically the influence of the incident angle of the exciting light on the SPPs launched by an atomic force microscope tip. We find that the amplitude and phase signals of these SPPs are best disentangled from other signals at grazing incident angle relative to the edge of the gold platelet. Furthermore, we introduce a simple model to extract the wavelength and in particular the propagation length of the tip-launched plasmons. Our experimental results are in excellent agreement with our theoretical model. The presented method allows the quantitative analysis of polaritons occurring in different materials at visible wavelengths.

1. Introduction

Surface plasmon polaritons (SPPs) can confine light in small volumes at the subwavelength scale [1]. SPPs are surface waves and are being investigated for various applications such as sensing [2], nanoplasmonic circuits [3], light generation [4,5] and photovoltaics [6]. To design and fabricate the optimal structures for these applications, it is important to know the complex wavevector, as its real part is inversely proportional to the plasmonic wavelength and its imaginary part inversely proportional to the propagation length [1].

Scattering-type scanning near-field optical microscopy (s-SNOM) [7] allows to explore surface waves with a spatial resolution down to a few tens of nanometers. In the past years, s-SNOM has been demonstrated to be a powerful tool to study polaritons of various kinds such as polaritons in two-dimensional (2D) materials [8,9] throughout the optical spectrum [10–15], in anisotropic materials [16,17] and SPPs on metals [18–20]. While the characterization of polaritons has been done in many works in the mid-infrared range [11–15], s-SNOM studies in the visible range are less common. s-SNOM measurements in the visible are indeed more challenging because the smaller extension of the light spot focused onto the atomic force microscope (AFM) tip makes the alignment more difficult and renders less stable scans. The study of surface waves in the visible is nevertheless relevant, as many polaritonic phenomena arise in this range [8–10,21]. In the case of SPPs on gold, the characterization of plasmonic slot waveguides has been achieved with a s-SNOM at telecom wavelengths [18,22] and the direct characterization of SPPs on a flat surface with an aperture-type SNOM has been achieved at 780 nm [23]. However, these works measured the SPPs in a transmission configuration, where the sample is illuminated from the bottom and

#454740 https://doi.org/10.1364/OE.454740
Journal © 2022 Received 26 Jan 2022; revised 10 Mar 2022; accepted 10 Mar 2022; published 17 Mar 2022

Optics EXPRESS

the AFM tip is used as a local scatterer to collect the near-field signal. This configuration is thus limited to substrates that are transparent at the excitation wavelength. By contrast, the characterization of SPPs in the reflection configuration offers more flexibility in the choice of substrate. Moreover, the transmission configuration requires the mediation of a well-defined scatterer to excite the SPPs, whereas in reflection the AFM tip itself acts as a scatterer to excite the SPPs. However, the characterization in reflection comes with the drawback that many excitation pathways are involved, which makes the near-field signal more difficult to analyze. One of these excitation paths is mediated by the sharp tip apex that provides the wavevector required to excite SPPs. These SPPs are called the tip-launched SPPs. Another excitation path is mediated by the sharp edges of the platelet that can also provide the required momentum for SPPs. SPP excitation by the edges is possible in gold since the SPPs have a weak confinement, in contrast to graphene [11,12,14]. In previous works [19,20], several SPP excitation pathways involving the platelet edge and the tip shaft have been identified. The SPPs excited or scattered at the edge are called edge-launched SPPs, and the ones reflected at the tip shaft are called tip-reflected edge-launched SPPs. All these SPPs can be identified through their interference patterns, and we showed in a previous study [20] that the wavelength of the tip-launched SPPs can be retrieved by isolating a region of the platelet free from edge-launched SPPs. However, the SPP propagation length is still to be quantified to fully characterize SPPs in the visible range and in reflection.

When analyzing surface waves in the reflection configuration, several studies [10,11,13–17] use the pseudo-heterodyne interferometric method [24] to suppress the far-field background and to obtain both the amplitude and phase of the near-field from their measurements. However, the full characterization of the surface waves is often done using either the real part of the field [14,16], where the amplitude and phase information have been merged, or only the near-field amplitude [10,17]. The independent use of the phase information as well as a simple model that could be used for the independent fitting and the comparison of the near-field amplitude and phase signals seem thus to be lacking.

Here, we perform near-field reflection measurements at visible wavelengths on monocrystalline gold platelets [25–31], that have shown to host better plasmonic properties compared to the common polycrystalline gold surfaces [32,33]. We isolate the clearest tip-launched SPPs when illuminating our sample with a laser beam impinging with a low azimuthal angle relative to the edge of the gold platelet. With the signal of the tip-launched SPPs, we develop a simple model for the amplitude and phase information, allowing us to determine with high confidence the wavelength as well as the propagation length of SPPs propagating at the surface of a monocrystalline gold platelet. To the best of our knowledge, this is the first time that the propagation length has been determined with a s-SNOM in reflection and in the visible. Furthermore, this model explains clearly the $\pi/2$ phase shift between the amplitude and phase signals observed in a previous study [34]. This full characterization of the complex SPP wavevector paves the way towards a broader understanding of the polaritonic phenomena in diverse materials [8–10,21]. Moreover, the proposed model helps to fundamentally understand the behaviour of s-SNOM amplitude and phase when studying surface waves in the reflection configuration.

2. Experimental details

An optical image of the sample measured in this study is shown in Fig. 1(a). More information about the sample can be found in the section 1 of Supplement 1. A sketch of its cross section is given in the inset. It consists of a monocrystalline gold platelet, synthesized by a wet-chemical synthesis process [26] and deposited on a 300 nm thermally grown silicon oxide layer. The darker branching line in the middle of the platelet is due to a fold of the platelet that has occurred during its deposition on the substrate. The propagation length of the SPPs on gold is typically about 4 times smaller [35] than the distance from the fold to the region of interest (ROI). Thus, this fold does not affect the SPPs on our ROI. The platelet under study is about 200 µm large. This is one

Optics EXPRESS

order of magnitude larger than the typical propagation length of our SPPs. Thus, interference between SPPs reflected from different edges can be avoided simply by scanning a region far from the platelet corners. A 2-nm aluminum oxide (Al_2O_3) layer has been deposited on the platelet by atomic layer deposition to protect the gold from impurities. The azimutal angle φ between the gold platelet's edge and the incident light is indicated in the figure.

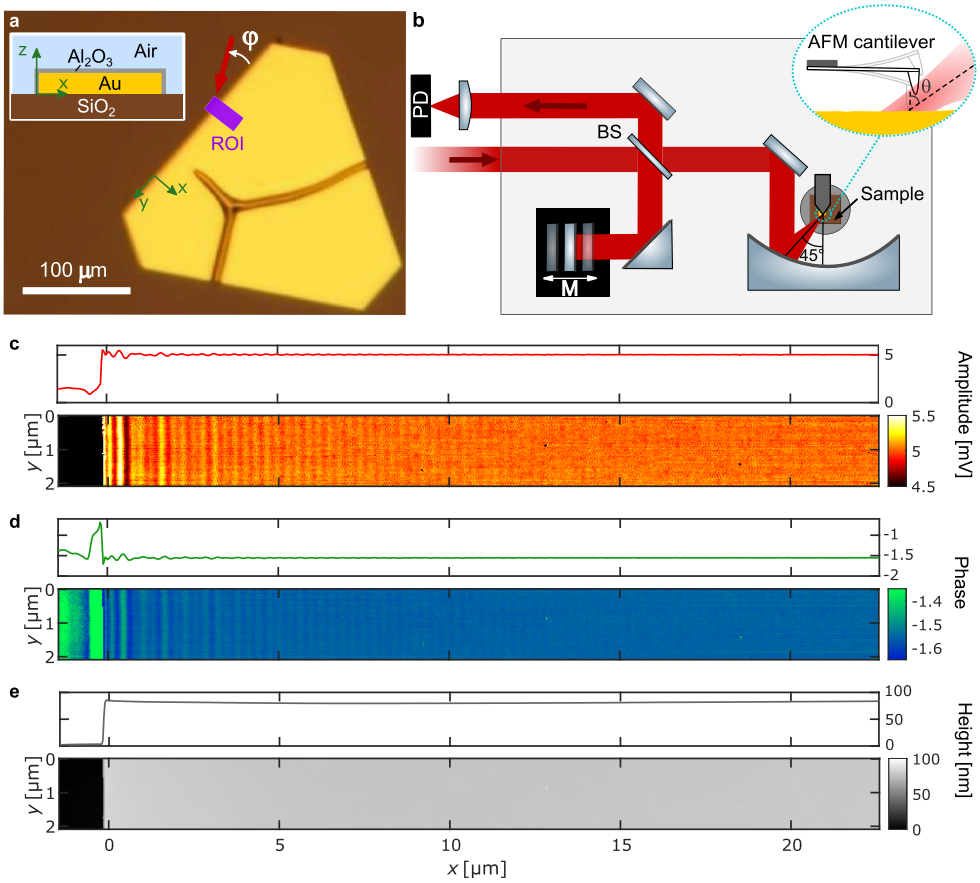

Fig. 1. Experimental setup and measurements. (a) Optical image of the sample under study. The incident light is represented by the red arrow and the azimuthal incident angle is represented by φ. The small violet rectangle close to the tip of the arrow indicates the scanned region. It is highlighted by the label "ROI" (region of interest). The inset displays a sketch of the sample and substrate cross-section. (b) Sketch of the s-SNOM setup. (c) Near-field amplitude, (d) near-field phase and (e) topography of the scanned region. The respective profiles are shown above each map and the origin of the x-axis is chosen to be at the platelet edge.

The s-SNOM setup used to characterize the SPPs is represented in Fig. 1(b). The light from a helium-neon laser at a wavelength of 633 nm is separated by a beam-splitter (BS) in two paths of equal intensity. One is focused on an AFM tip oscillating above the sample. The other is directed towards a reference mirror oscillating at a frequency M = 300 Hz, necessary for the pseudo-heterodyne interferometric detection [24]. The field scattered at the tip then interferes with the reference field and is detected by a photodiode (PD). Demodulating the total signal enables to retrieve the amplitude and phase of the near-field, as well as to strongly suppress the

Optics EXPRESS

interference with the far-field background [24]. More information about the setup can be found in the section 2 of Supplement 1.

The topography, amplitude and phase maps resulting from one of our measurements are displayed in Fig. 1(c)-(e). The topography presented in Fig. 1(e) gives a sample thickness of about 90 nm. The platelets are thus thick enough to allow us to neglect any possible hybridization between modes propagating at the air/gold and silica/gold interfaces [20,36]. The sample root-mean-square (RMS) roughness extracted from this Fig. 1(e) is about 200 pm, attesting for a very high surface quality. Note that the platelet edge - placed at the x-axis origin - is sharp and without defect: this is important to avoid additional perturbations of the propagating wavefront pattern. The near-field optical amplitude and phase are shown respectively in Fig. 1(c) and 1(d). The scales have been adjusted to visualize the SPP interference patterns better. Line profiles are extracted from these maps by averaging the signal over 200 pixels in the y-direction. The respective profiles are displayed above the maps. On the gold surface, SPP interference patterns superimposed on a constant field offset are visible up to about 15 µm, both in the near-field amplitude and the near-field phase maps.

3. Results and discussions

3.1. Influence of the light incidence

Figure 2(a)-(c) present the profiles extracted from three measurements where the azimutal angle φ has been varied, with $\varphi = -3°$, $-136°$ and $-93°$, respectively. For clarity, the profiles are normalized and shown on a restricted interval of 15 µm. The measurements of three other angles can be found in the section 4 of Supplement 1. The three figures show a region closer to the edge with a complex interference pattern, and another region - highlighted by the red background - with more regular damped sinusoidal oscillations. The first region is characterized by the interference between the tip-launched SPPs, the edge-launched SPPs and the tip-reflected edge-launched SPPs [20]. Because the edge-launched and tip-reflected edge-launched SPPs are present only when the incident light illuminates the edge, the length of the edge region (white background) is taken as always larger than the width of the diffraction-limited spot of the incoming light projected onto the sample at a polar angle of $\theta = 60°$. The Fourier transforms of the amplitude profiles are displayed as the black curves in Fig. 2(d)-(f). To make the small fringe spacing more apparent, the resulting spectra are plotted as a function of the fringe spacing $\Lambda = 2\pi/K$ instead of the spatial frequency components K. By considering only the interference of each type of SPP with a strong constant field and neglecting higher-order interference effects such as the interference between the different SPP paths [20], several peaks can be recognized. The peaks at the shortest wavelength are the peaks of interest corresponding to the tip-launched SPPs at a wavelength Λ_{tl}, given by [14,19,20]

$$\Lambda_{\mathrm{tl}} = \frac{\lambda_{\mathrm{SPP}}}{2} = \frac{\lambda_0}{2\Re(\tilde{n})} = \frac{2\pi}{K_{\mathrm{tl}}} \tag{1}$$

where $\tilde{n}$ is the effective complex refractive index of SPPs at the air/Al_2O_3/gold interface, $\Re(\tilde{n})$ is its real part and λ_0 is the wavelength of the incident light in vacuum. Since it is directly launched by the tip, Λ_{tl} is independent of the incident angle. Other peaks can be found at the wavelengths of the edge-launched SPPs, $\Lambda_{el1/el2}$ and the wavelength of the tip-reflected edge-launched SPPs, Λ_{trel}. Using the phase-matching condition along the platelet edge and approximating the incident wave as a plane wave, these edge-launched SPP wavelengths have been found to be expressed as [19,20]

$$\Lambda_{el1/el2}(\theta,\varphi) = \frac{\lambda_0}{-\sin(\theta)\sin(\pm\varphi) + \sqrt{\sin^2(\theta)\sin^2(\pm\varphi) - \sin^2(\theta) + \Re(\tilde{n})^2}}, \tag{2}$$

where the + sign is used for Λ_{el1} and the − sign for Λ_{el2}. The tip-reflected edge-launched SPP wavelength is expressed as $\Lambda_{trel} = \Lambda_{el1}(\theta', \varphi)$, where θ' depends on the reflection angle of the

Optics EXPRESS

incident light at the tip. More information about the different SPP wavelengths and interference paths can be found in our previous work [20]. To calculate the value of these wavelengths for the different incident angles, we use as reference values the tabulated frequency-dependent refractive index of gold from McPeak *et al.* [35] of $\varepsilon_g(633\text{ nm}) = -13.02 + 1.033i$ and the one of Al_2O_3 from M. Tulio Aguilar-Gama *et al.* [37] of $\varepsilon_{Al_2O_3}(633\text{ nm}) = 2.62$. The value of the gold refractive index has been chosen over other tabulated values [38,39] as it was giving the longest SPP propagation length at this wavelength. Solving the dispersion relation for the multilayer system [1] composed of air, Al_2O_3 and gold gives the complex SPP wavevector $\beta_{SPP} = (10.37 + 0.03662i)\ \mu m^{-1}$, thus $\Re(\tilde{n}) = \Re(\beta_{SPP}/k_0) = 1.045$. Using this last value and Eqs. (1) and (2), the different SPP wavelengths can be determined. These wavelengths are displayed as vertical lines in Fig. 2(d)-(f). In Fig. 2(d) - corresponding to the grazing incident angle - the tip-launched peak at $\Lambda_{tl}^{th} = 0.303$ µm is very prominent, while the peaks at about $\Lambda_{el1}(60°, -3°) = 1.0$ µm, $\Lambda_{el2}(60°, -3°) = 1.17$ µm and $\Lambda_{trel}(35°, -3°) = 0.71$ µm can barely be recognized. However, for incident angles of $\varphi = -136°$ in Fig. 2(e) and $\varphi = -93°$ in Fig. 2(f), peaks at $\Lambda_{el1}(60°, -136°) = 0.44$ µm and $\Lambda_{el1}(60°, -93°) = 0.33$ µm, as well as a smaller tip-launched peak at Λ_{tl}^{th}, can be identified in the corresponding Fourier transforms. The large linewidth of the edge-launched contribution can be explained by the fact that Eq. (2) is valid for an illumination by a plane wave with concomitant spatially constant intensity. In our case the beam is focused on the tip with a numerical aperture of 0.37, thereby exciting SPPs propagating with different angles with respect to the normal of the edge of the platelet. Furthermore, the intensity of the excitation beam at the edge changes while scanning due to the Gaussian profile of the laser beam.

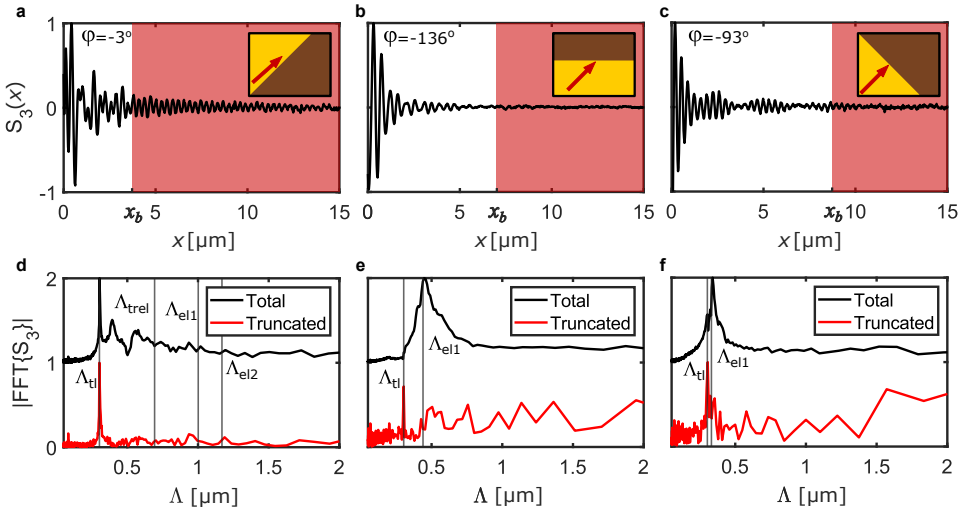

Fig. 2. Angle dependency of the different SPPs. (a)-(c) Near-field amplitude profiles of the scanned region on the gold platelets at grazing angle ($\varphi = -3°$), at $\varphi = -136°$ and at $\varphi = -93°$, respectively. The red areas starting at the value x_b indicate the portion of the curve where the tip-launched plasmons dominate the signal. The insets depict a top view of the sample edge for each measurement. The red arrow represents the incident light. (d)-(f) represent the fast Fourier transforms (FFT) of (a)-(c), respectively, as a function of the fringe spacing $\Lambda = 2\pi/K$. The red curve is the FFT of the data in the red area of (a)-(c), demonstrating a clear tip-launched plasmon peak at grazing angle.

The Fourier transform of the truncated profiles located in the red-shaded areas in Fig. 2(a)-(c) are represented by the red curves in Fig. 2(d)-(f). As has been highlighted recently [20], selecting

Optics EXPRESS

the data far from the edges has the effect of filtering out the contribution from the edge-launched SPPs and isolating the tip-launched SPPs, thus leaving a clearer tip-launched peak. However, the significance of this filtering effect is angle dependent. For the angles $\varphi = -136°$ and $\varphi = -93°$, truncating has indeed the effect of highly suppressing the peak at Λ_{el1} in Fig. 2(e) and 2(f). However, compared to the truncated profile at grazing azimutal angle, only a very small and noisy tip-launched peak remains. The RMS of the noise amplitude for Λ between 0.1 and 0.2 µm in the truncated profile of Fig. 2(d) is indeed about 20 times smaller than the tip-launched peak, while only about 5 to 7 times smaller in Fig. 2(e) and 2(f). Furthermore, in Fig. 2(f), the peak at Λ_{el1} is present close to the tip-launched peak. These two effects hinder the proper fitting of the tip-launched peak, and thus the characterization of the tip-launched plasmons at these incident angles.

The comparison between the different incident angles highlights that the tip-launched SPPs could be best retrieved using the measurement at grazing angle. This angle dependency could be explained by an anisotropic excitation of the SPPs by the tip. Previous results [19] have indeed reported an angle-dependent generation of the tip-launched SPPs, due to the non-circular symmetry of the commercial tip used in their s-SNOM. In the aforementioned study, the angle for which the tip-launched plasmons could be seen best has been identified as the perpendicular incidence, i.e. $\varphi = 90°$. The ideal angle is different in our case, as our tip has a different shape than the one used in Ref. [19]. Therefore, we assign the difference in the ideal angle to the difference in tip shape.

As a clear tip-launched plasmon peak is needed for the full characterization of the complex wavevector, in the following we will focus our analysis of the SPP properties on the measurement at grazing angle, in the restricted region where only the tip-launched SPPs are present.

3.2. Model for the detected SPPs

Figure 3(a) displays the near-field amplitude and phase profiles of the s-SNOM measurement at grazing azimutal angle $\varphi = -3°$, in the region where only the tip-launched SPPs are present. Both profiles show similar sinusoidal oscillations, with an apparent relative shift between the near-field phase and amplitude by a distance of about $\Lambda_{\mathrm{tl}}/4$, corresponding to a phase of $\pi/2$. Besides having been observed in a previous study [34], this $\pi/2$ shift is also confirmed by the good overlap between the two curves when shifting the near-field phase curve by $-\pi/2$, as presented in Fig. 3(b).

To explain this phase difference, we introduce a model that considers the interference between the tip-launched SPPs, described as a circular wave, E_{tl}, and a constant field E_g. Because the tip-launched SPPs travel two times the tip-edge distance at each scanning position, the corresponding plasmonic field is described by an apparent wavevector $K_{\mathrm{tl}} = 2\Re(\beta_{SPP})$ which is twice larger than the actual wavevector, $\Re(\beta_{SPP})$. This also means that we observe an apparent propagation length of the field $L_{\mathrm{p}}^{\mathrm{tl}} = 1/(2\Im(\beta_{SPP}))$ that is two times smaller than the actual one. $E_g = |E_g|e^{i\phi_g}$, with $|E_g|$ its constant amplitude and ϕ_g its constant phase, corresponds to the constant offsets seen on the gold surface in the experimental profiles in Fig. 1(c) and 1(d). Our model does not assume anything about the nature of this constant field. However, as the pseudo-heterodyne detection removes the far-field background due to the incident light [24,40], E_g is understood as the near-field coming from the portion of the light back-scattered directly from the sample surface towards the AFM tip [14]. This effect can be considered as constant because our gold platelets are extremely flat. With these two contributions, the total near field is $E_{NF} = E_{tl} + E_g$. From the experimental profiles, we observe that typically $|E_g|$ is indeed constant and much larger than the SPP oscillation amplitude A (see the amplitude profile in Fig. 1(c)). Further analysis gives values of E_g that are typically 40 times larger than A.

In addition, we only consider a range of positions from about 3 µm - to avoid the contributions from the edge SPPs - to about 30 µm - where the oscillations cannot be differentiated from the

Optics EXPRESS

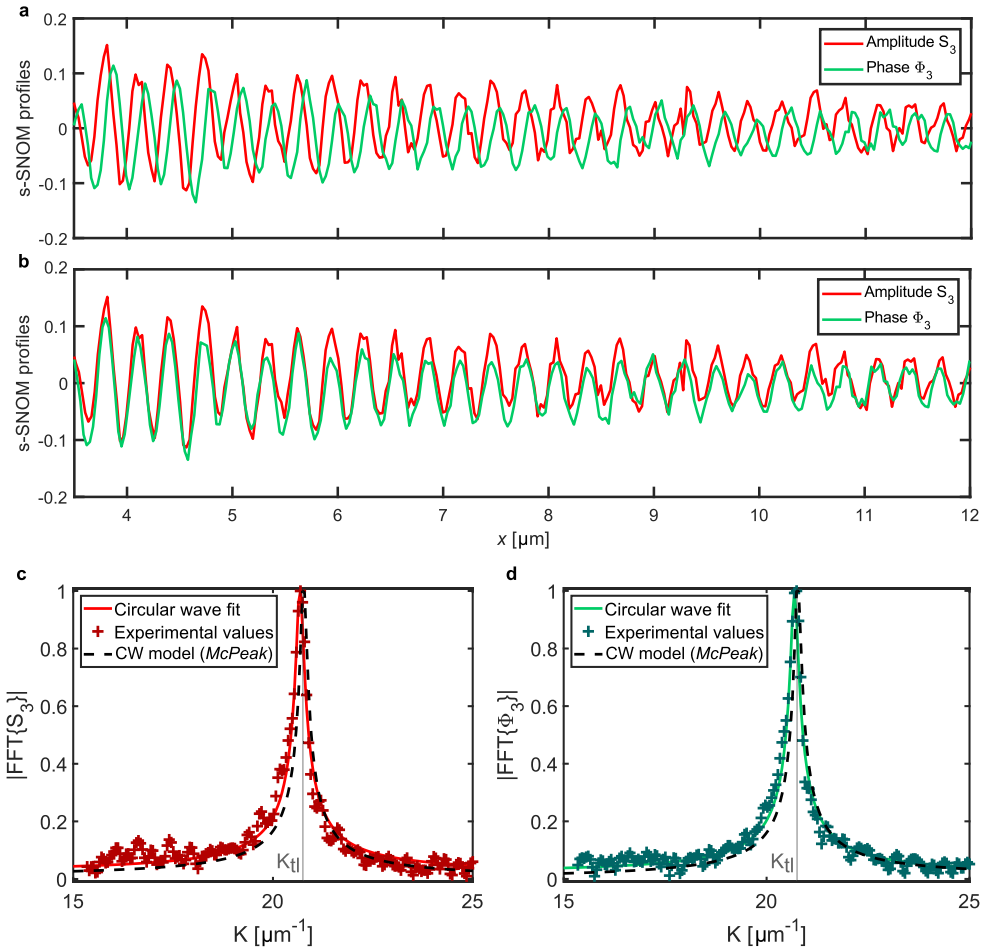

Fig. 3. Amplitude and phase at grazing azimutal angle. (a) Comparison of the amplitude and phase profiles at grazing angle. (b) Same profiles with the near-field phase shifted by $-\pi/2$. (c) Fit of the tip-launched SPPs' amplitude peak visible in Fig. 2(b). The CW model curve refers to the FFT of a circular wave (here Eq. (3)) where the refractive index from McPeak *et al.* [35] has been used. (d) Fit of the corresponding phase data.

Optics EXPRESS

noise anymore. Using a Taylor expansion in $A/(\sqrt{x}|E_g|)$ of the total amplitude expression and keeping the first-order terms of this Taylor expansion, one can find that (see Supplement 1 Section 5.B)

$$|E_{NF}| \approx |E_g| + \frac{A}{\sqrt{x}} e^{-x/L_p^{tl}} \cos\left(K_{tl}x - \phi\right), \tag{3}$$

where ϕ is a constant phase consisting of the sum of a plasmonic phase constant ϕ_p due to the reflection at the edge and the gold phase constant ϕ_g. Using the same principle, the total phase of the near-field can obtained as follows (see Supplement 1 Section 5.C)

$$\Phi_{NF} \approx \frac{A}{|E_g|\sqrt{x}} e^{-x/L_p^{tl}} \sin\left(K_{tl}x - \phi\right) + B, \tag{4}$$

where B is a constant depending on the value of ϕ_g and on the average optical path difference between the near-field and the reference field [24,40]. The derivation of these expressions and of the $\pi/2$ relative phase shift can be found in the section 5 of Supplement 1. Since the resulting expressions feature a cosine dependence of the total amplitude and a sine dependence of the total phase, the $\pi/2$ shift can be seen as a direct consequence of the interference between the strong constant field and the SPPs.

In addition to highlight in a unambiguous way the $\pi/2$ shift between the near-field amplitude and phase, these expressions have the advantage of being simple enough to be used as fitting functions, meaning that the amplitude and the phase signals can be fitted separately, both in real space and in k-space. While fitting the near-field amplitude or real part of the near-field is fairly common in s-SNOM studies of polaritons [10,14,17], no independent fitting of the near-field phase has been done so far. As the information extracted from the near-field phase is essentially the same as the near-field amplitude, the two fits can be compared to verify the accuracy of the corresponding parameter values. Note that fitting in k-space has the advantages of displaying the extracted information in a concise manner through a single resonance, and of filtering out the noise at other frequencies.

Defining $S_3 = |E_{NF}| - |E_g|$ and $\Phi_3 = \Phi_{NF} - B$, the discrete Fourier transform of the near-field data can be fitted. Because the tip-launched SPPs are circular waves and we are using the fast Fourier transform (FFT) algorithm on the measurement profiles, the peak is not expected to be a Lorentzian. An analytical expression of the Fourier transform of a circular wave can be found and has been used to find the SPP wavelength on gold in a previous study [41]. However, this analytical expression is not valid for a circular wave profile truncated at the starting value x_b (see Supplement 1 Section 6). For this reason, we chose to fit numerically the signals in k-space. The description of the fitting procedure can be found in the section 3 of Supplement 1. The Fourier transform of the experimental data and the circular wave fit are plotted in Fig. 3(c) and 3(d) for the amplitude and phase information, respectively. The fit of the near-field amplitude and phase for the starting value of the truncated segment $x_b = 4.02$ µm, and its comparison with the fit in real space, are summarized in Table 1. The uncertainties when fitting in k-space are slightly larger, but still comparable to the uncertainties in real space.

Table 1. Comparison of values for the wavevector $K_{tl} = 2\pi/\Lambda_{tl}$ and propagation length L_p^{tl}, as obtained in real space and in Fourier space, for one starting value x_b.

	Amplitude profile		Phase profile		McPeak *et al.*
	k-space	Real space	k-space	Real space	
K_{tl} (µm^{-1})	20.658 ± 0.009	20.662 ± 0.003	20.674 ± 0.007	20.674 ± 0.009	20.75
L_p^{tl} (µm)	12 ± 1	12.5 ± 0.4	12 ± 1	11.9 ± 0.3	13.65

These values could vary with the choice of x_b. This starting value has to be sufficiently large to avoid the signal from the edge-launched and tip-reflected edge-launched SPPs, but also

Optics EXPRESS

sufficiently small to cover as much of the tip-launched SPP signal as possible. Once these two criteria are fulfilled, there still can be some slight changes in the extracted values due to noise that depends on the choice of x_b. After studying systematically the evolution of the fitting parameters with x_b, we find that our fitting procedure is stable with regard to the choice of x_b (see Supplement 1 Section 7).

We compare the values of our fitting parameters with theoretical calculations taking into account values of the refractive index for gold and Al_2O_3 found in the literature [35,37] (see Table 1). The FFT of circular waves obtained with these reference values - integrated over the same range as curves of the circular wave fit - are plotted in dashed lines in Fig. 3(c) and 3(d). While being close, the experimental values are slightly different from the calculated ones, up to about 15% lower in the case of the propagation length. These discrepancies can be explained by a slightly different experimental refractive index than the one from the literature. Indeed, different studies characterizing gold [35,38,39] have provided slightly different refractive indices. In addition, the refractive index of Al_2O_3 taken from the literature corresponds to a layer of 50 nm of Al_2O_3, while we have only 2 nm. This could also induce a difference in the refractive index of our sample.

We have thus shown that with our method it is possible to extract both the real and imaginary parts of the complex wavevector of our SPPs simultaneously, in excellent agreement with our theoretical model and values found in the literature.

4. Conclusion

In this work, we have identified the grazing azimutal angle as the best configuration to isolate the tip-launched SPPs. At this particular angle, the near-field amplitude and, for the first time, phase could be fitted. To obtain the expressions for the fitting functions, we have developed a model for the interference between these tip-launched SPPs and a field that we approximated to be a constant. The equations derived for the fitting procedure explicitly justify the damped sinusoidal behaviour of the near-field amplitude and phase, and the $\pi/2$ shift between them. It should be noted that the structures of Eqs. (3) and (4) do not depend on the material and are valid as long as the amplitude of the plasmonic oscillations is much smaller than the amplitude of the constant field. Our analysis could thus be applied to a whole range of other materials hosting different types of polaritons.

With our method, we obtain, for the first time to our knowledge using a s-SNOM in reflection configuration, values of both the gold SPPs wavelength, $\Lambda_{\mathrm{tl}} = 304,0$ nm, and propagation length, $L_{\mathrm{p}}^{\mathrm{tl}} = 12$ µm, corresponding to about 40 coherent oscillations. These values are consistent between the near-field amplitude and phase, do not sensitively depend on the choice of interval used for the fit and are in excellent agreement with previous values found in the literature. Furthermore, our measurements confirm the high surface quality of the monocrystalline gold platelets. With the Al_2O_3 protection layer, we reproduced our results after eight months (see Supplement 1 Section 7), which shows the stability of our sample. This full characterization of the SPPs provides a better quantitative understanding of their interactions with other materials. Quantitative study of polaritons in reflection and in the visible is thus facilitated. With the possibility to measure the complex-valued wavevector of polaritons, this work opens the door to the exploration of quantum related phenomena in polariton physics [21,42,43] at the nanometer scale, at visible frequencies and irrespective of the type of substrate.

Funding. Danmarks Grundforskningsfond (DNRF103, DNRF147); Villum Fonden (00028233); Natur og Univers, Det Frie Forskningsråd (0135-00403B); Teknologi og Produktion, Det Frie Forskningsråd (9041-00333B).

Acknowledgments. The authors thank E. Schatz from NanoStruct GmbH for the fabrication of the sample and for valuable discussions. The authors also thank L. Giannini for his help with the s-SNOM measurements at different incident angles. L.N.C. thanks M. Fischer and M. A. Jørgensen for valuable discussions about the fitting methods and theory.

Disclosures. The authors declare no conflicts of interest.

Optics EXPRESS

Note. During the revision process of this manuscript, a similar recent preprint was brought to our attention [44]. The authors use similar monocrystalline gold platelets to study the propagation length of SPPs excited at the edge of the platelets, for 5 different excitation wavelengths and in a transmission configuration. Although the configuration and the data processing is different from our work, the authors obtained a value of the propagation length in good agreement with our results.

Data availability. Data underlying the results presented in this paper are not publicly available at this time but may be obtained from the authors upon reasonable request.

Supplemental document. See Supplement 1 for supporting content.

References

1. S. A. Maier, *Plasmonics: Fundamentals and Applications* (Springer Science & Business Media, 2007).
2. S. Roh, T. Chung, and B. Lee, "Overview of the characteristics of micro-and nano-structured surface plasmon resonance sensors," Sensors **11**(2), 1565–1588 (2011).
3. J.-S. Huang, V. Callegari, P. Geisler, C. Brüning, J. Kern, J. C. Prangsma, X. Wu, T. Feichtner, J. Ziegler, P. Weinmann, M. Kamp, A. Forchel, P. Biagioni, U. Sennhauser, and B. Hecht, "Atomically flat single-crystalline gold nanostructures for plasmonic nanocircuitry," Nat. Commun. **1**(1), 150 (2010).
4. S. Schmidt, B. Piglosiewicz, D. Sadiq, J. Shirdel, J. S. Lee, P. Vasa, N. Park, D.-S. Kim, and C. Lienau, "Adiabatic nanofocusing on ultrasmooth single-crystalline gold tapers creates a 10-nm-sized light source with few-cycle time resolution," ACS Nano **6**(7), 6040–6048 (2012).
5. J. Kern, R. Kullock, J. Prangsma, M. Emmerling, M. Kamp, and B. Hecht, "Electrically driven optical antennas," Nat. Photonics **9**(9), 582–586 (2015).
6. V. E. Ferry, J. N. Munday, and H. A. Atwater, "Design considerations for plasmonic photovoltaics," Adv. Mater. **22**(43), 4794–4808 (2010).
7. F. Keilmann and R. Hillenbrand, "Near-field microscopy by elastic light scattering from a tip," Phil. Trans. R. Soc. A **362**(1817), 787–805 (2004).
8. D. Basov, M. Fogler, and F. G. De Abajo, "Polaritons in van der waals materials," Science **354**(6309), aag1992 (2016).
9. T. Low, A. Chaves, J. D. Caldwell, A. Kumar, N. X. Fang, P. Avouris, T. F. Heinz, F. Guinea, L. Martin-Moreno, and F. Koppens, "Polaritons in layered two-dimensional materials," Nat. Mater. **16**(2), 182–194 (2017).
10. F. Hu, Y. Luan, M. Scott, J. Yan, D. Mandrus, X. Xu, and Z. Fei, "Imaging exciton-polariton transport in mose2 waveguides," Nat. Photonics **11**(6), 356–360 (2017).
11. J. Chen, M. Badioli, P. Alonso-González, S. Thongrattanasiri, F. Huth, J. Osmond, M. Spasenović, A. Centeno, A. Pesquera, P. Godignon, P. Godignon, A. Z. Elorza, N. Camara, F. J. G. de Abajo, R. Hillenbrand, and F. H. L. Koppens, "Optical nano-imaging of gate-tunable graphene plasmons," Nature **487**(7405), 77–81 (2012).
12. Z. Fei, A. Rodin, G. O. Andreev, W. Bao, A. McLeod, M. Wagner, L. Zhang, Z. Zhao, M. Thiemens, G. Dominguez, M. M. Fogler, A. H. C. Neto, C. N. Lau, F. Keilmann, and D. N. Basov, "Gate-tuning of graphene plasmons revealed by infrared nano-imaging," Nature **487**(7405), 82–85 (2012).
13. S. Dai, Z. Fei, Q. Ma, A. Rodin, M. Wagner, A. McLeod, M. Liu, W. Gannett, W. Regan, K. Watanabe, T. Taniguchi, M. Thiemens, G. Dominguez, A. H. C. Neto, A. Zettl, F. Keilmann, P. Jarillo-Herrero, M. M. Fogler, and D. N. Basov, "Tunable phonon polaritons in atomically thin van der waals crystals of boron nitride," Science **343**(6175), 1125–1129 (2014).
14. A. Woessner, M. B. Lundeberg, Y. Gao, A. Principi, P. Alonso-González, M. Carrega, K. Watanabe, T. Taniguchi, G. Vignale, M. Polini, J. Hone, R. Hillenbrand, and F. H. L. Koppens, "Highly confined low-loss plasmons in graphene–boron nitride heterostructures," Nat. Mater. **14**(4), 421–425 (2015).
15. A. Bylinkin, M. Schnell, M. Autore, F. Calavalle, P. Li, J. Taboada-Gutièrrez, S. Liu, J. H. Edgar, F. Casanova, L. E. Hueso, P. Alonso-Gonzalez, A. Y. Nikitin, and R. Hillenbrand, "Real-space observation of vibrational strong coupling between propagating phonon polaritons and organic molecules," Nat. Photonics **15**(3), 197–202 (2021).
16. W. Ma, P. Alonso-González, S. Li, A. Y. Nikitin, J. Yuan, J. Martín-Sánchez, J. Taboada-Gutiérrez, I. Amenabar, P. Li, S. Vélez, C. Tollan, Z. Dai, Y. Zhang, S. Sriram, K. Kalantar-Zadeh, S.-T. Lee, R. Hillenbrand, and Q. Bao, "In-plane anisotropic and ultra-low-loss polaritons in a natural van der waals crystal," Nature **562**(7728), 557–562 (2018).
17. J. Taboada-Gutiérrez, G. Álvarez-Pérez, J. Duan, W. Ma, K. Crowley, I. Prieto, A. Bylinkin, M. Autore, H. Volkova, K. Kimura, T. Kimura, M.-H. Berger, S. Li, Q. Bao, X. P. A. Gao, A. Y. Errea Ion, Nikitin R. Hillenbrand, J. Martín-Sánchez, and P. Alonso-González, "Broad spectral tuning of ultra-low-loss polaritons in a van der waals crystal by intercalation," Nat. Mater. **19**(9), 964–968 (2020).
18. A. Andryieuski, V. A. Zenin, R. Malureanu, V. S. Volkov, S. I. Bozhevolnyi, and A. V. Lavrinenko, "Direct characterization of plasmonic slot waveguides and nanocouplers," Nano Lett. **14**(7), 3925–3929 (2014).
19. F. Walla, M. M. Wiecha, N. Mecklenbeck, S. Beldi, F. Keilmann, M. D. Thomson, and H. G. Roskos, "Anisotropic excitation of surface plasmon polaritons on a metal film by a scattering-type scanning near-field microscope with a non-rotationally-symmetric probe tip," Nanophotonics **7**(1), 269–276 (2018).

Optics EXPRESS

20. K. J. Kaltenecker, E. Krauss, L. Casses, M. Geisler, B. Hecht, N. A. Mortensen, P. U. Jepsen, and N. Stenger, "Mono-crystalline gold platelets: a high-quality platform for surface plasmon polaritons," Nanophotonics **9**(2), 509–522 (2020).
21. D. Basov, A. Asenjo-Garcia, P. J. Schuck, X. Zhu, and A. Rubio, "Polariton panorama," Nanophotonics **10**(1), 549–577 (2021).
22. M. Prämassing, M. Liebtrau, H. Schill, S. Irsen, and S. Linden, "Interferometric near-field characterization of plasmonic slot waveguides in single-and poly-crystalline gold films," Opt. Express **28**(9), 12998–13007 (2020).
23. A. Sierant, B. R. Jany, and T. Kawalec, "Near-field characterization of surface plasmon polaritons on a nanofabricated transmission structure," Phys. Rev. B **103**(16), 165433 (2021).
24. N. Ocelic, A. Huber, and R. Hillenbrand, "Pseudoheterodyne detection for background-free near-field spectroscopy," Appl. Phys. Lett. **89**(10), 101124 (2006).
25. X. Wu, R. Kullock, E. Krauss, and B. Hecht, "Single-crystalline gold microplates grown on substrates by solution-phase synthesis," Cryst. Res. Technol. **50**(8), 595–602 (2015).
26. E. Krauss, R. Kullock, X. Wu, P. Geisler, N. Lundt, M. Kamp, and B. Hecht, "Controlled growth of high-aspect-ratio single-crystalline gold platelets," Cryst. Growth Des. **18**(3), 1297–1302 (2018).
27. S. Boroviks, C. Wolff, J. Linnet, Y. Yang, F. Todisco, A. S. Roberts, S. I. Bozhevolnyi, B. Hecht, and N. A. Mortensen, "Interference in edge-scattering from monocrystalline gold flakes," Opt. Mater. Express **8**(12), 3688–3697 (2018).
28. S. Boroviks, F. Todisco, N. A. Mortensen, and S. I. Bozhevolnyi, "Use of monocrystalline gold flakes for gap plasmon-based metasurfaces operating in the visible," Opt. Mater. Express **9**(11), 4209–4217 (2019).
29. S. Boroviks, T. Yezekyan, Á. R. Echarri, F. J. G. de Abajo, J. D. Cox, S. I. Bozhevolnyi, N. A. Mortensen, and C. Wolff, "Anisotropic second-harmonic generation from monocrystalline gold flakes," Opt. Lett. **46**(4), 833–836 (2021).
30. B. Munkhbat, A. Canales, B. Küçüköz, D. G. Baranov, and T. O. Shegai, "Tunable self-assembled casimir microcavities and polaritons," Nature **597**(7875), 214–219 (2021).
31. B. Frank, P. Kahl, D. Podbiel, G. Spektor, M. Orenstein, L. Fu, T. Weiss, M. Horn-von Hoegen, T. J. Davis, F.-J. M. Zu Heringdorf, and H. Giessen, "Short-range surface plasmonics: Localized electron emission dynamics from a 60-nm spot on an atomically flat single-crystalline gold surface," Sci. Adv. **3**(7), e1700721 (2017).
32. R. Méjard, A. Verdy, O. Demichel, M. Petit, L. Markey, F. Herbst, R. Chassagnon, G. Colas-des Francs, B. Cluzel, and A. Bouhelier, "Advanced engineering of single-crystal gold nanoantennas," Opt. Mater. Express **7**(4), 1157–1168 (2017).
33. B. Hoffmann, M. Bashouti, T. Feichtner, M. Mačković, C. Dieker, A. Salaheldin, P. Richter, O. Gordan, D. Zahn, E. Spiecker, and S. Christiansen, "New insights into colloidal gold flakes: structural investigation, micro-ellipsometry and thinning procedure towards ultrathin monocrystalline layers," Nanoscale **8**(8), 4529–4536 (2016).
34. Y. Li, N. Zhou, E. C. Kinzel, X. Ren, and X. Xu, "The origin of interferometric effect involving surface plasmon polariton in scattering near-field scanning optical microscopy," Opt. Express **22**(3), 2965–2972 (2014).
35. K. M. McPeak, S. V. Jayanti, S. J. P. Kress, S. Meyer, S. Iotti, A. Rossinelli, and D. J. Norris, "Plasmonic films can easily be better: Rules and recipes," ACS Photonics **2**(3), 326–333 (2015).
36. M. Großmann, M. Black, J. Jaruschewski, A. Klick, T. Leißner, J. Fiutowski, H.-G. Rubahn, and M. Bauer, "Micro-spectroscopy of buried short-range surface plasmon polaritons supported by thin polycrystalline gold films," Plasmonics **16**(3), 737–746 (2021).
37. M. T. Aguilar-Gama, E. Ramírez-Morales, Z. Montiel-González, A. Mendoza-Galván, M. Sotelo-Lerma, P. Nair, and H. Hu, "Structure and refractive index of thin alumina films grown by atomic layer deposition," J. Mater. Sci.: Mater. Electron. **26**, 5546–5552 (2015).
38. P. B. Johnson and R.-W. Christy, "Optical constants of the noble metals," Phys. Rev. B **6**(12), 4370–4379 (1972).
39. R. L. Olmon, B. Slovick, T. W. Johnson, D. Shelton, S.-H. Oh, G. D. Boreman, and M. B. Raschke, "Optical dielectric function of gold," Phys. Rev. B **86**(23), 235147 (2012).
40. J. M. Atkin, S. Berweger, A. C. Jones, and M. B. Raschke, "Nano-optical imaging and spectroscopy of order, phases, and domains in complex solids," Adv. Phys. **61**(6), 745–842 (2012).
41. K. J. Kaltenecker, S. Rao DS, M. Rasmussen, H. B. Lassen, E. J. Kelleher, E. Krauss, B. Hecht, N. A. Mortensen, L. Grüner-Nielsen, C. Markos, O. Bang, N. Stenger, and P. U. Jepsen, "Near-infrared nanospectroscopy using a low-noise supercontinuum source," APL Photonics **6**(6), 066106 (2021).
42. S. Boroviks, Z.-H. Lin, V. A. Zenin, M. Ziegler, A. Dellith, P. Gonçalves, C. Wolff, S. I. Bozhevolnyi, J.-S. Huang, and N. A. Mortensen, "Extremely confined gap plasmon modes: when nonlocality matters," arXiv preprint arXiv:2111.07561 (2021).
43. M. S. Tame, K. McEnery, Ş. Özdemir, J. Lee, S. A. Maier, and M. Kim, "Quantum plasmonics," Nat. Phys. **9**(6), 329–340 (2013).
44. Y. Lebsir, S. Boroviks, M. Thomaschewski, S. I. Bozhevolnyi, and V. A. Zenin, "Ultimate limit for optical losses in gold, revealed by quantitative near-field microscopy," arXiv:2203.00754 [physics.optics] (2022).